Available online at www.sciencedirect.com

ScienceDirect

Proceedings of the Combustion Institute 37 (2019) 5437–5444

Proceedings of the Combustion Institute

www.elsevier.com/locate/proci

Soot and flow field in turbulent swirl-stabilized spray flames of Jet A-1 in a model combustor

Lu-Yin Wang, Cody K. Bauer, Ömer L. Gülder*

University of Toronto Institute for Aerospace Studies, 4925 Dufferin Street, Toronto, Ontario M3H 5T6, Canada

Received 1 December 2017; accepted 17 May 2018
Available online 23 June 2018

Abstract

Soot production processes and their interaction with the swirling flow field were studied experimentally in turbulent spray flames in a model gas turbine combustor. Two Jet A-1/air spray flames with two different air flow rates both with constant fuel flow corresponding to a thermal power of 10 kW were stabilized in the combustor with a swirl number of 0.55. Soot measurements were collected using auto-compensating laser-induced incandescence and velocity measurements were obtained using stereoscopic particle image velocimetry techniques. The particle image velocimetry displayed a distinct change in spray pattern from a V-shaped hollow cone to a V-shaped solid cone when the air flow rate was increased. The first soot event was not detected until 30 mm above the combustor inlet was reached, which was expected as it was necessary for liquid fuel to disperse and evaporate. The flow field featured strong inner and outer recirculation zones as well as the inner and outer shear layers. Soot concentration distributions were found to be confined to the outside of the inner recirculation zone; this is in contrast to the gaseous fuel swirl-stabilized flames in which soot particles are mainly detected within the inner recirculation zone. Time-averaged maximum soot volume fraction level decreased by about 60% with a 20% increase in air mass flow rate instigated by enhanced oxidation rate and turbulent mixing. The primary soot particle size was found to fall in the range of 30 and 60 nm for both cases. The results obtained emphasize the role played by the intermittent structures and air flow rate on soot processes in swirling spray combustion. Observed soot distributions in liquid spray flames in this work differ drastically from those reported previously for gaseous fuel combustion in swirl-stabilized flames.

Keywords: Swirl-stabilized flames; Turbulent spray combustion; Soot in Jet A-1 flame; Combustion of Jet A-1 spray; Primary soot particle size

1. Introduction

Soot emissions from combustion devices used in transportation, power production, and other industrial applications are of significant interest because of harmful effects of soot on the well-being

* Corresponding author.
E-mail addresses: ogulder@utias.utoronto.ca, flame-utias7@usa.net (Ö.L. Gülder).

https://doi.org/10.1016/j.proci.2018.05.093
1540-7489

of humans and the environment. To develop a better understanding of soot formation remains as a challenging problem due to its complex chemistry in non-premixed laminar flames; the situation is compounded further in non-premixed turbulent flames as the turbulence, chemistry, and transport processes are interacting in a manner whose underlying principles have not been firmly established yet. For this reason most of the soot research has been focused on laminar flames to improve the understanding of the formation mechanisms in the absence of turbulence, although the flames are turbulent in practically all combustion devices [1]. It has been shown that the unsteady laminar non-premixed flames yield a significantly higher soot volume fraction than their equivalent but steady counterparts having the same mean fuel flow rate [2,3], pointing to the potential effects the turbulence and intermittency would have on the soot processes. In a gaseous fuel turbulent jet flame it was demonstrated that the fraction of time of observing soot particles at a given measurement location is a few percent due to intermittency [4]. Similar observations showing the strong spatial and temporal intermittency of soot formed in turbulent flames have been reported in swirl stabilized gaseous fuel flames with laser-induced incandescence (LII) measurements of soot [5,6]. Although the studies in gaseous fuel piloted jet flames and gaseous swirl-stabilized burners have been contributing to the improvement of the understanding of soot processes in non-premixed turbulent combustion [4–7,9–14,8], less is known, however, about the soot processes in swirl-stabilized combustors burning liquid fuels [15]. The current investigation aims to fill this gap in soot processes in swirl-stabilized spray flames through measurements of the flow field, soot concentrations, and the primary soot particle sizes in a model gas turbine combustor fueled with aviation fuel Jet A-1.

Swirl-stabilized combustion is widely used in practical devices where the recirculating fluid is generally composed of hot unburnt fuel, combustion products and chemically active radicals. The high turbulence intensity that prevails in the recirculation zones, allows for a rapid transfer of heat and radicals to the in-flowing reactants from the recirculating fluids. This mechanism leads to easy ignition of reactants and consequently, flame stabilization over a wide range of flow conditions. Development and use of numerical schemes capable of estimating the features of the flow field and pollutant formation is one of the avenues adopted by the gas turbine industry; however, currently available numerical schemes are not at a level to have soot processes computed to yield acceptable results [16]. The improvement of the numerical schemes hinges on the availability of validation-suited data obtained from laboratory-scale combustors operating at relevant conditions. As a consequence, information on the soot processes in swirl-stabilized model combustors with well-defined operating conditions is highly desirable.

The scope of the current study encompasses an investigation of soot production in two Jet A-1 spray flames with different air flow rates established in a swirl flow model combustor with optical access. Flow fields and the soot concentrations, along with soot particle sizes, are measured using stereoscopic particle image velocimetry (SPIV) and auto-compensating LII (AC-LII) techniques, respectively. Soot concentration distributions within the combustor are presented and discussed in relation to the corresponding swirling flow field.

2. Experimental methodology

2.1. Burner setup

The combustor, in which the Jet A-1 spray flames were stabilized, is similar to the one described by Meier et al. [17], but with a longer chamber and with a liquid fuel nozzle in the centerbody at the combustor dump-plane to create a spray flame, Fig. 1. The combustion chamber is enclosed by four quartz windows to allow optical access, and has a dimension of $94 \times 94 \times 188$ mm^3 where the aspect ratio of 2:1 is required to handle the spray flames. A conical converging tunnel leads to a central exhaust pipe with a diameter of 40 mm. The air at room temperature passes through a radial swirler consisting of 12 vanes and enters the burner through an annular nozzle with an inner diameter of 5 mm and an outer diameter of 27.85 mm. A commercial pressure-swirl nozzle (Delavan, spray pattern of semi-solid cone, spray angle of 60°) was used to atomize the liquid Jet A-1 fuel. The air and fuel nozzles are located at the inlet of the combustion chamber, and the measured swirl number is about 0.55. Air and Jet A-1 flow rates of the two spray flames, each with a thermal power of 10 kW, are summarized in Table 1. The air and liquid Jet A-1 fuel flow rates were controlled by calibrated flow controllers (Brooks SLA 5853 and Alicat LCS-100SCCM). The uncertainty of the Brooks and Alicat flow controllers are $\pm 1\%$ of the set flow rate and $\pm 2\%$ of the full scale flow rate, respectively.

Table 1
Summary of the experimental conditions; P_t is the thermal power, Re the exit Reynolds number of the air flow, $\dot{m}_f$ the fuel flow rate, $\dot{m}_a$ the air flow rate and ϕ_g the global equivalence ratio.

Case	P_t (kW)	Re	$\dot{m}_f$ (g/s)	$\dot{m}_a$ (g/s)	ϕ_g
R1	10	19600	0.22	5.8	0.55
R2	10	23300	0.22	6.9	0.47

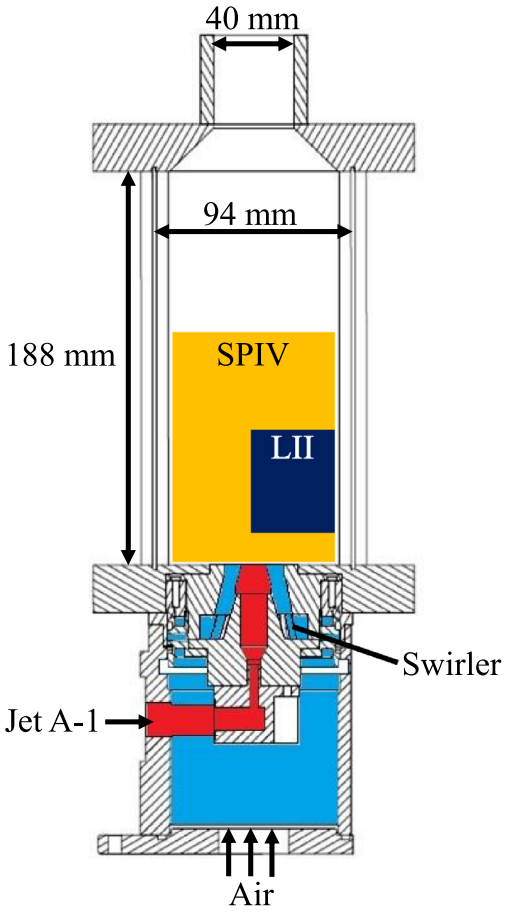

Fig. 1. Cross-sectional view of the burner assembly. Yellow box indicates the region mapped by the planar measurement of SPIV, and dark blue box shows the region probed by the point measurement of LII. (For interpretation of the references to color in this figure legend, the reader is referred to the web version of this article.)

The fuel flow rates in the reacting cases were chosen such that the flame was confined and the fluctuation in the spray pattern was negligible.

It should be noted that, in contrast to actual gas turbine engine combustors, the model combustor adopted for the current study has a square cross-section. The square cross-section creates typical corner vortices or recirculation zones that furnish a cylindrical boundary for the flow [18], mimicking the geometry of the gas turbine combustors. As a consequence, the flow physics information obtained from square cross-section combustors can be extended to actual gas turbine combustors. From an experimental rig design perspective, square cross-sections allow an affordable design and construction, in addition to providing full optical access for laser diagnostics. For these advantages, a square-cross section model gas turbine

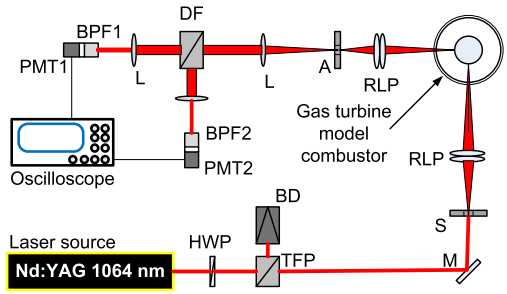

Fig. 2. Layout of the laser-induced incandescence instrument. A – aperture; BD – beam dump; BPF – band-pass filter (#1 is 440 nm; #2 is 692 nm); DF – dichroic filter; HWP – half-wave plate; L – lens (150 mm); M – mirror; PMT – photomultiplier tube; RLP – relay lens pair (250 mm); S – slit (3 mm $\times$ 100 μm) ; TFP – thin film polarizer.

combustor was used for the current experimental study on sooting turbulent swirl flames of Jet A-1.

2.2. Soot measurement

Soot volume fractions and primary soot particle sizes were measured using AC-LII which was calibrated by an integrating sphere with a known radiance-wavelength curve as described in Snelling et al. [19]. The quasi-axisymmetric feature of the combustor allowed us to concentrate our soot measurement zone in one half of the combustor. To heat the soot particles, a 1064 nm pulsed Nd:YAG laser (multimode Continuum Surelite I-10) was used to avoid the strong absorption of polycyclic aromatic hydrocarbons (PAHs) near the visible and ultraviolet spectra which could lead to an overestimation of soot volume fraction.

The laser was operated at 10 Hz with a maximum output energy of 200 mJ/pulse and a pulse duration of 5 ns. A combination of a half wave plate and a thin film polarizer shown in Fig. 2 was used to attenuate the laser beam energy to an appropriate laser fluence of about 0.1 J/cm^2, at which the soot sublimation is insignificant and the measurement remains non-intrusive [20]. The laser beam was shaped into a top-hat spatial profile by a 3 mm $\times$ 100 μm ceramic vertical slit and was focused to the test location through a 250 mm relay lens pair. The short-lived incandescence emitted from the heated soot particles was captured by a pair of photomultiplier tubes (Hamamatsu, rise time of 1.4 ns) at two distinct wavelengths of 440 nm and 692 nm. The soot analysis was performed on a section of the LII signals which was chosen from 25 ns to 125 ns after the peak to avoid the contributions from the quick-cooling PAHs. The soot particle temperature is inferred based on the two-color pyrometry principle. The fluctuations observed in soot temperature decay signals with time (not shown) would impact the uncertainty of

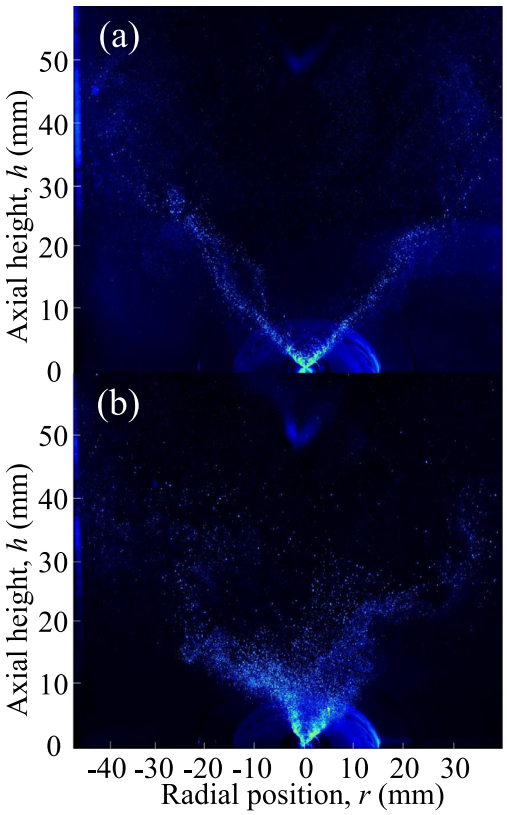

Fig. 3. Examples of instantaneous fuel spray particle images: (a) R1 and (b) R2. The quarter circle seen at the radial position 10–15 mm is a light reflection developed within the air nozzle.

the measurements. The magnitude of the potential uncertainty introduced by temperature fluctuations is included in the Monte-Carlo simulation reported in Section 3 of the paper. The absolute soot volume fraction is obtained from the soot particle temperature and the absolute LII intensity using the following expression [19]:

$$f_v = \frac{V\,\lambda^6\left(\exp\left[\frac{hc}{k\lambda T}\right]-1\right)}{\eta\, G\, 12\pi c^2 h\, w\, E(m_\lambda)} \tag{1}$$

where V is the voltage response of the detector to the LII signal; λ is the detection wavelength; T is the effective particle temperature; η is the calibration factor; w is the equivalent laser sheet thickness; G is the detector gain voltage; $E(m_\lambda)$ is the soot absorption function; h is the Planck's constant; c is the speed of light and k is the Boltzmann's constant.

2.3. Velocity measurement

The planar measurement of three dimensional velocity fields were obtained using a 6 Hz SPIV system under the identical test conditions with AC-LII experiments. The air flow was seeded with 1 μm titanium dioxide particles which was illuminated by a 532 nm double-pulsed Nd:YAG laser (Litron Laser, Nano-L PIV) with a maximum pulse energy of 200 mJ/pulse. The laser beam was formed into a laser sheet of 60 mm height using a combination of two cylindrical lens and one spherical lens. The laser pulse separation was set between 30 μs and 80 μs depending on the flow condition to obtain optimal particle displacements. A pair of CCD cameras (LaVision Imager pro X, 2048 × 2048 pixel^2, 14 bit), each mounted with a macro lens (Nikon, f = 105 mm, f/8.0), was used to capture the scattering of light from the seeding particles and fuel droplets. Each lens was equipped

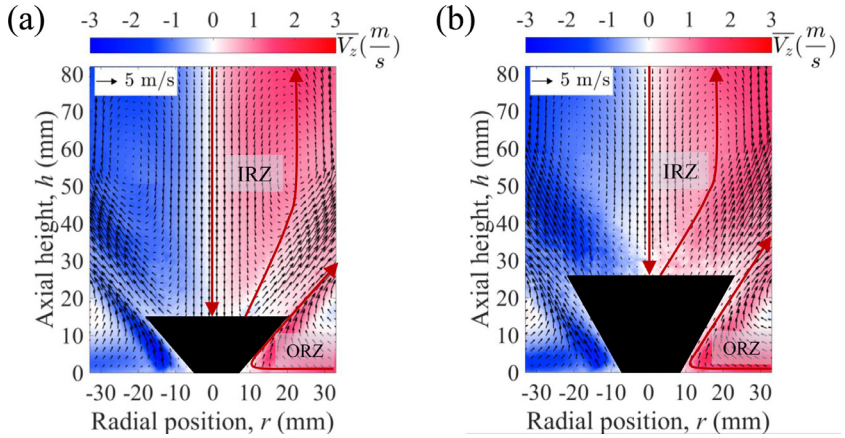

Fig. 4. Time-averaged velocity fields for cases (a) R1 and (b) R2. Vectors indicate the axial and radial velocity components and the colored contours indicate the out-of-plane velocity component. Reference vector in the top left corner at each image represents a velocity vector of 5 m/s.

with a 532 nm bandpass filter with 1 nm bandwidth to reduce the influence from the flame luminosity and droplet scattering. Additional neutral density filter was also used from case to case to suppress the strong light scattered by the droplets. The Scheimpflug adapter was installed on each camera to achieve the coincidence of the laser sheet with the camera focal plane. For each flow condition, 2000 image pairs were acquired over 5 experimental runs of 400 image pairs to avoid window contamination from the seeding particles. A multi-pass vector calculation technique (DaVis 8.3) was used on each image pair with the interrogation box size decreasing from 64×64 pixels^2 with 75% overlap to 32×32 pixels^2 with 50% overlap. The resulting final vector spacing is about 0.7 mm.

3. Results and discussion

3.1. Flow field

A representative instantaneous particle image for each case taken from the SPIV measurements is displayed in Fig. 3. The strong light scattered from the fuel droplets shows that the spray pattern switched from a distinct V-shaped hollow cone in case R1 to a V-shaped solid cone in case R2. This difference in droplet spatial distribution caused the flame in case R2 to be stabilized at a higher height above the nozzle. During the post-processing steps, the fuel region in each image pair was masked out to calculate the gas phase velocity, and vice versa. The fuel droplet velocity was computed when only the region inside the fuel mask was considered. The combined time-averaged velocity distributions from fuel and gaseous regions for cases R1 and R2 are shown in Fig. 4. In case R2, the mean velocity field in the region between $h = 20$ mm and $h = 30$ mm downstream of the fuel nozzle near the combustor centerline contains several null readings causing a non-smooth field. This is due to the insufficient amount of fuel droplets in that region, and thus the cross-correlation algorithm failed to find a definite peak velocity in the interrogation box. This issue became less severe in case R1 because the fuel droplets were more concentrated in the V-shaped cone.

The flow features consist of a high-velocity cone-shaped inflow stream, pronounced inner and outer recirculation zones (IRZ, ORZ) as well as the corresponding inner and outer shear layers (ISL, OSL), which can be observed in all cases. However, there are noticeable differences in the flow field between isothermal (not shown) and reacting cases. Qualitatively, the azimuthal velocity within the inflow stream becomes more pronounced and the angle of the conical air inflow stream decreases in the isothermal cases leading to a narrower IRZ and a larger ORZ. The addition of swirling fuel stream restricts the space for air flow to expand radially inward and thus the IRZ widens. The location where the fuel stream meets the recirculating flow in case R1 is about $h = 10$ mm, but this location shifts up to about $h = 30$ mm in case R2, resulting in a smaller IRZ.

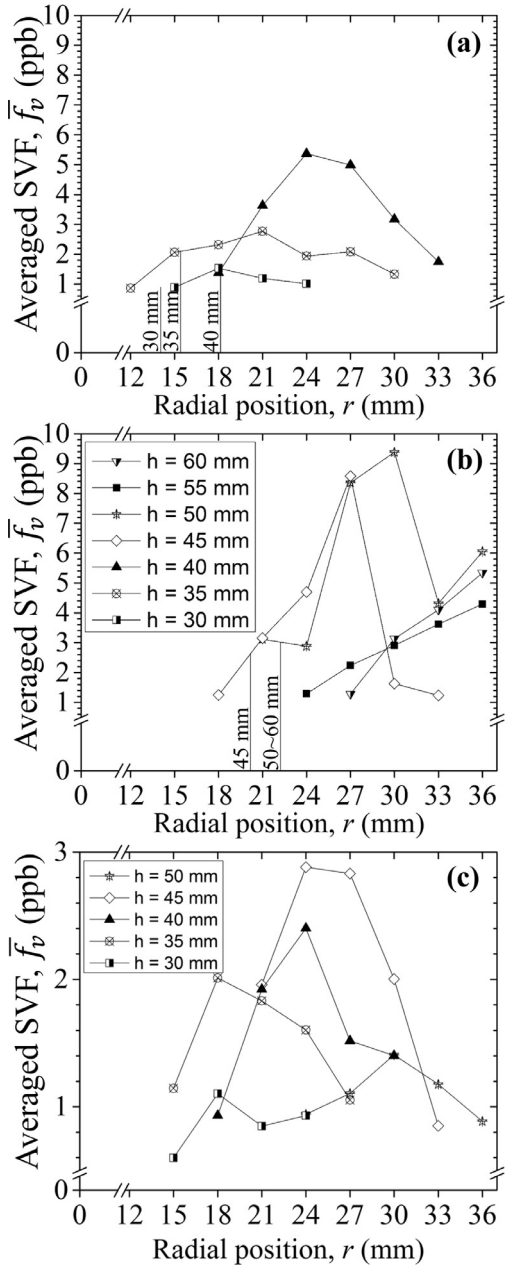

Fig. 5. Radial profiles of the time-averaged soot volume fraction for case R1 shown in (a) and (b), and case R2 shown in (c). Vertical lines indicate the location of ISL for case R1. Vertical lines are not shown in (c) for case R2 since all soot measurements were found to be outside of IRZ. Radial position of 0 mm corresponds to the centerline of the combustor. SVF = soot volume fraction.

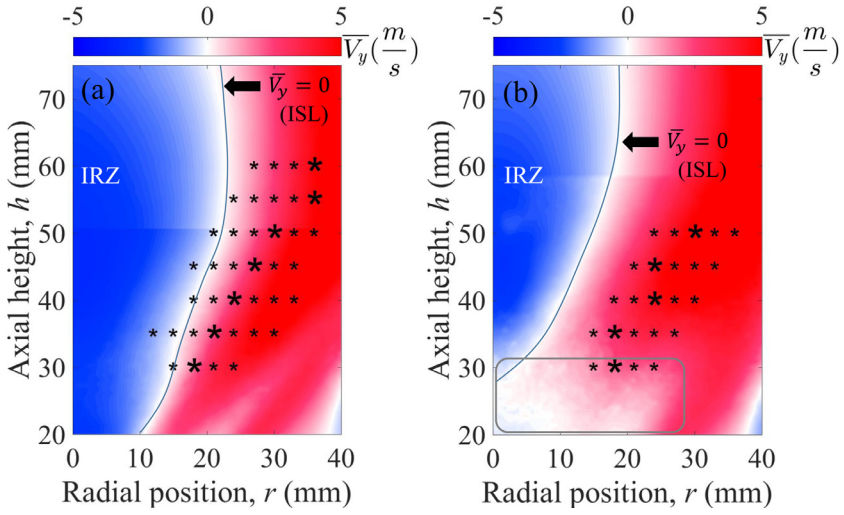

Fig. 6. Contour plots of the mean axial velocity for cases (a) R1 and (b) R2. Markers indicate the locations at which soot events were detected with larger markers showing the positions of the maximum time-averaged soot volume fraction at each axial height. The grey rectangular box marks the region where the velocity calculations were strongly affected by the fuel droplets.

The overall flow field appears to be fairly symmetric which justifies our AC-LII experiments performed in one half of the flames. It should be noted that the effects of distortion on particle images, caused by the refractive index variations due to the unavoidable strong temperature gradient in the flame zone, was occasionally observed and the quality of the particle images were improved using several non-linear and time-series filters.

3.2. Soot volume fraction

At each location, 12000 laser shots for AC-LII measurements were performed from which the soot volume fractions, f_v, were inferred using Eq. (1). Unlike similar soot measurements done in laminar flames where each laser shot at a sooting location produces a LII signal, most laser shots in turbulent flames do not intersect with any soot particle due to the high level of intermittency. For the studied flames, the probability of finding a soot signal is about 1% to 4% for case R1, and about 0.5% to 1% for case R2. The resulting time-averaged soot volume fraction distribution, $\bar{f}_v$, computed by multiplying f_v with the signal probability, is presented in Fig. 5. In case R1, the time-averaged soot volume fraction reaches its maximum of about 9.4 ppb at $h = 50$ mm and $r = 30$ mm. In case R2, the maximum soot volume fraction decreases to about 2.9 ppb at $h = 45$ mm and $r = 24$ mm. By increasing the air mass flow rate by about 20%, the overall soot concentration in case R2 is observed to be about 60% lower than that in case R1. The higher air flow rate is expected to reduce the residence time for soot precursors to nucleate and form primary soot particles as well as to enhance the soot oxidation process resulting in a lower soot volume fraction.

The radial profile of case R1 shows that the peak soot volume fraction shifts from $r = 18$ mm to $r = 36$ mm as the axial height increases from 30 mm to 55 mm, Fig. 5. This trend of a radially outward shift with increasing height can also be observed, though not as distinct, in case R2. Additionally, the radial profiles in case R1 and R2 show an initial increase in soot concentration as a function of axial height followed by a rapid drop after the height of 50 mm and 45 mm, respectively. It should be noted that no soot events are detected in the region below 30 mm height where the fuel droplets exist in abundance leading to a condition unfavourable to soot formation. An important observation is that soot particles are located mainly outside of the IRZ in both spray flames, Fig. 5. This can be seen clearly in Fig. 6; star markers indicate the locations at which soot events were detected with larger markers showing the positions of the maximum time-averaged soot volume fraction at each axial height. This observation is in stark contrast to what was found in swirling gaseous flames reported previously in the literature [6,9,8] where soot particles were mainly found within the IRZ. The scarcity of soot signals in the IRZ in the spray flames arises from two potential causes: (a) the shape of the liquid spray with a nominal cone angle of 60° distributes the fuel droplets radially, and (b) there is a finite time for droplets to evaporate before the soot initiating and forming pyrolysis reactions initiate, by which time droplets reach the IRZ boundary and cross it.

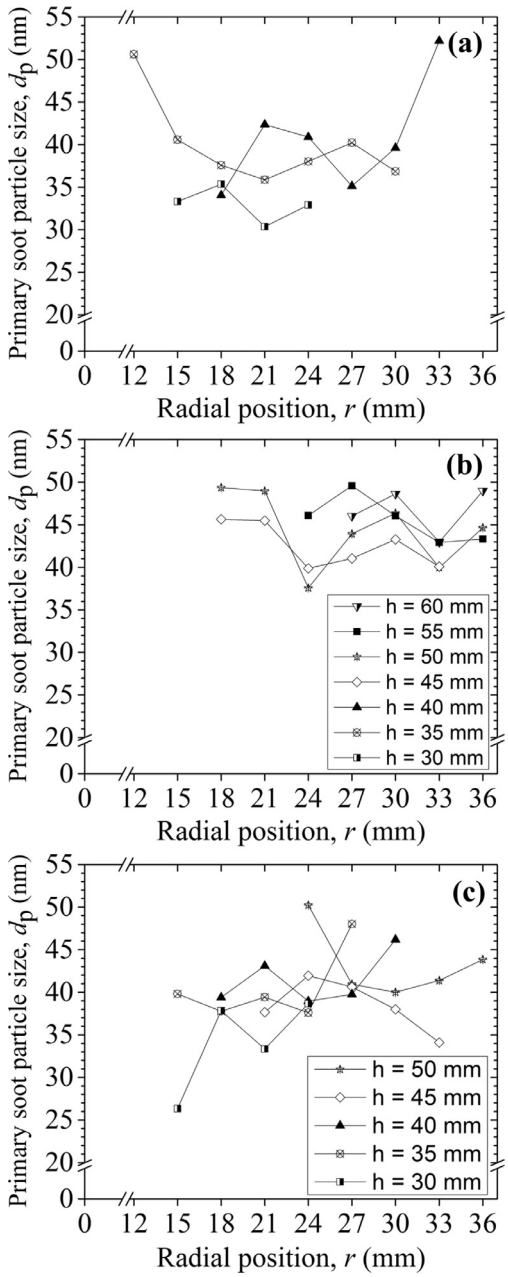

Fig. 7. Radial profiles of the primary soot particle size for case R1 shown in (a) and (b), and case R2 shown in (c). Radial position of 0 mm corresponds to the centerline of the combustor.

The uncertainty of the soot volume fraction originating from the systematic errors in each term in Eq. (1) was estimated using a Monte-Carlo simulation similar to the method described in [21]. The histogram of f_v retrieved from 10000 iterations is fitted with a log-normal distribution and the resulting total uncertainty of f_v spans between −48% (2.5 percentile) and 55% (97.5 percentile) of the mean value.

3.3. Primary soot particle size

The primary soot particle diameter is derived from the LII signal based on the heat conduction model in transition regime by McCoy and Cha [22]. Resulting primary soot particle size distributions are shown in Fig. 7. Unlike soot volume fraction, the primary soot particle diameter does not exhibit a strong dependence on the air mass flow rate, nor does it display a clear trend of particle size growth in either radial or axial direction. The primary particle diameters are found largely in the range of 30–50 nm. In a similar study conducted in the same swirl-stabilized combustor geometry [9], but with a shorter combustor length, using ethylene as the fuel yielded slightly smaller primary soot particle sizes than the current results. Although the overall equivalence ratio was much smaller than the current cases, the soot volume fractions were much higher with ethylene as the fuel.

Using the Monte-Carlo simulation, the histogram of primary soot particle size retrieved from 10000 iterations is fitted with a normal distribution and the resulting total uncertainty of d_p falls within $\pm$ 27% of the mean value. A separate analysis was done by varying only the local gas temperature. The resulting uncertainty in d_p falls within $\pm$ 15% of the mean value, which reveals that the uncertainty in the gas temperature plays a major role in determining the primary soot particle diameter.

4. Conclusions

The soot formation, growth and oxidation were studied experimentally in a model gas turbine combustor. Two turbulent non-premixed Jet A-1/air swirl-stabilized flames at atmospheric pressure with different air mass flow rates of 5.8 and 6.9 g/s were measured using laser-induced incandescence for soot concentrations and stereoscopic particle image velocimetry for velocity fields. The flow field exhibited a typical swirl-stabilized flame feature consisting of the inner and outer recirculation zones and their corresponding inner and outer shear layers. A comparison between the reacting and non-reacting flow fields suggested a wider inner recirculation zone and a smaller outer recirculation zone in the presence of spray combustion. The spray pattern in the case of lower air flow rate was close to a V-shaped hollow cone, and changed to a V-shaped solid cone in the case of higher air flow rate. The soot growth was observed from the axial height of 30 mm to 50 mm for the low air flow rate case, and from the axial height of 30 mm to 45 mm for the high air flow rate case. The majority of the soot particles were found outside the inner recirculation

zone; this is in contrast to the gaseous fuel swirl-stabilized flames in which soot concentrations are mainly found within the inner recirculation zone. It was found that when the air mass flow rate increased by 20%, from case R1 to case R2, the maximum soot concentration decreases by about 60%, pointing to the significant influence of turbulence and air flow rate on soot processes . However, the primary soot particle sizes, whose diameters ranged from about 30 nm to 50 nm, showed a weak dependence on the air flow rate.

Acknowledgments

We thank the Ontario Research Fund for a Research Excellence Program grant (ORF RE07-034) awarded to the senior author.

References

[1] A.E. Karataş, Ö.L. Gülder, *Prog. Energy Combust. Sci.* 38 (2012) 818–845.
[2] C. Shaddix, K. Smyth, *Combust. Flame* 107 (1996) 418–452.
[3] S.B. Dworkin, J.A. Cooke, B.A.V. Bennett, et al., *Combust. Theory Model.* 13 (2009) 795–822.
[4] N. Qamar, Z. Alwahabi, Q. Chan, G. Nathan, D. Roekaerts, K. King, *Combust. Flame* 156 (2009) 1339–1347.
[5] K.P. Geigle, M. Köhler, W. O'Loughlin, W. Meier, *Proc. Combust. Inst.* 35 (2015) 3373–3380.
[6] K.P. Geigle, R. Hadef, M. Stöhr, W. Meier, *Proc. Combust. Inst.* 36 (2017) 3917–3924.
[7] M. Köhler, K.P. Geigle, W. Meier, B.M. Crosland, K.A. Thomson, G.J. Smallwood, *Appl. Phys. B* 104 (2011) 409–425.
[8] S. Chatterjee, C. Halmo, Ö.L. Gülder, Structure of the velocity and soot concentrations fields of a swirl-stabilized turbulent non-premixed flame in a gas turbine model combustor. ASME India Gas Turbine Conference: Paper GTINDIA 2014-8114, 2014.
[9] S. Chatterjee, Ö.L. Gülder, *Exp. Thermal Fluid Sci.* 95 (2018) 73–80.
[10] A. Attili, F. Bisetti, M.E. Mueller, H. Pitsch, *Combust. Flame* 161 (2014) 1849–1865.
[11] D. Bartos, M. Dunn, M. Sirignano, A. D'Anna, A.R. Masri, *Proc. Combust. Inst.* 36 (2017) 1869–1876.
[12] D. Gu, Z. Sun, B.B. Dally, P.R. Medwell, Z.T. Alwahabi, G.J. Nathan, *Combust. Flame* 179 (2017) 33–50.
[13] O. Park, R.A. Burns, O.R. Buxton, N.T. Clemens, *Proc. Combust. Inst.* 36 (2017) 899–907.
[14] S. Mahmoud, G. Nathan, Z. Alwahabi, Z. Sun, P. Medwell, B. Dally, *Proc. Combust. Inst.* 36 (2017) 889–897.
[15] T.R. Meyer, S. Roy, V.M. Belovich, E. Corporan, J.R. Gord, *Appl. Opt.* 44 (2005) 445–454.
[16] V. Raman, R.O. Fox, *Annu. Rev. Fluid Mech.* 48 (2016) 159–190.
[17] W. Meier, I. Boxx, M. Stöhr, C. Carter, *Exp. Fluids* 49 (2010) 865–882.
[18] V.L. Okulov, V.G. Meledin, I.V. Naumov, *Tech. Phys.* 48 (2003) 1249–1254.
[19] D.R. Snelling, G.J. Smallwood, F. Liu, Ö.L. Gülder, W.D. Bachalo, *Appl. Opt.* 44 (2005) 6773–6785.
[20] H. Michelsen, C. Schulz, G. Smallwood, S. Will, *Prog Energy Combust. Sci.* 51 (2015) 2–48.
[21] B. Crosland, K. Thomson, M. Johnson, *Appl. Phys. B* 112 (2013) 381–393.
[22] B.J. McCoy, C.Y. Cha, *Chem. Eng. Sci.* 29 (1974) 381–388.